

EVIDENCE FOR THE TWO FLUID SCENARIO IN SOLAR PROMINENCES

E. WIEHR¹, G. STELLMACHER², AND M. BIANDA³

Draft version April 3, 2019

ABSTRACT

This paper presents observational evidence of the different dynamical behavior of neutral and ionized species in solar prominences. The analysis of a time-series of Sr II 4078 Å and Na D spectra in a quiescent prominence yields systematically larger Doppler shifts (line-of-sight velocities) for the ions $V_{LOS}(\text{Sr II}) = 1.22 \times V_{LOS}(\text{Na D})$. Both lines show a 30 minutes oscillation of good coherence. Sixteen hours later the same prominence underwent marked morphological changes (with a rising dome), and the Sr II velocity excess drops to $V_{LOS}(\text{Sr II}) = 1.11 \times V_{LOS}(\text{Na D})$. The same excess is found for the line pair Fe II 5018 Å and He I 5015 Å. The widths of the ionic lines, mainly non-thermally broadened, are not related to the macro velocities. The emission ratio of Na D and Sr II, a measure of the electron density, yields $n_e = 4 \times 10^{10} \text{ cm}^{-3}$, shows no relation with the V_{LOS} variation or with height above the limb, and seems to be reduced 16 hr later during the active phase. We apply a new wavelength reference from aureola spectra, which is independent of photospheric velocity fields.

Subject headings: techniques spectroscopic - methods observational - Sun prominences

1. INTRODUCTION

The different dynamical behavior of neutral and ionized species has been receiving increasing attention recently. It can well be studied in solar prominences because, due to their relatively low temperature of $T \leq 10^4 \text{ K}$, they represent a partially ionized and weakly collisional plasma with a considerable number of neutrals (e.g., Gilbert et al., 2002). Numerical simulations indicate that the decoupling of neutral and ionized species in the solar atmosphere can give rise to non-ideal MHD effects that can result, for instance, in heating caused by the friction between the two species, modify the equilibrium of magnetic structures, introduce instabilities under certain magnetic configurations, or change the way the various wave modes transform into each other and propagate through the atmosphere (see the review by Ballester et al., 2018).

Motivated by these considerations different observers tried to measure differences between the line-of-sight velocities (LOS) of ions and neutrals. From simultaneous time-series spectra, Anan et al. (2017) found no conclusive differences, whereas Khomeiko et al. (2016) found differences only at restricted locations with high velocities in short-lived transients. Stellmacher & Wiehr (2017), on the contrary, found systematically larger LOS velocities for ions (Sr II, Fe II) than for neutral atoms (Na I and He I), whereas a comparison between neutrals (H, He) gives a 1:1 relation. The conspicuous similarities between the spectra of Sr II 4078 and Na D suggest that these lines share the same dynamical behavior within a common resolution element (in those data about $1.5'' \times 1.5''$). In order to investigate this behavior in more detail, we discuss new observations of the faint metallic lines Sr II 4078 and Na D. These are optically thin and can be expected to respond quite selectively to 'hot' or 'cold' plasma conditions because Sr ionizes above $\approx 9000 \text{ K}$, where neutral Na hardly exists.

2. OBSERVATIONS

From the Locarno observatory (IRSOL) we observed a quiescent prominence at the west limb, 5° north, on 2017 June 24-26. Its appearance on June 24 as a disk filament shows that the prominence is inclined to the limb by $\approx 45^\circ$ (Figure 1). The two emission lines Sr II 4077.71 Å and Na D₂ 5889.95 Å are taken in the 13th and 9th orders, respectively, at a fixed grating angle. A simple change of two pre-filters separating the orders allows monitoring of both lines at almost the same position on the CCD (Figure 2).

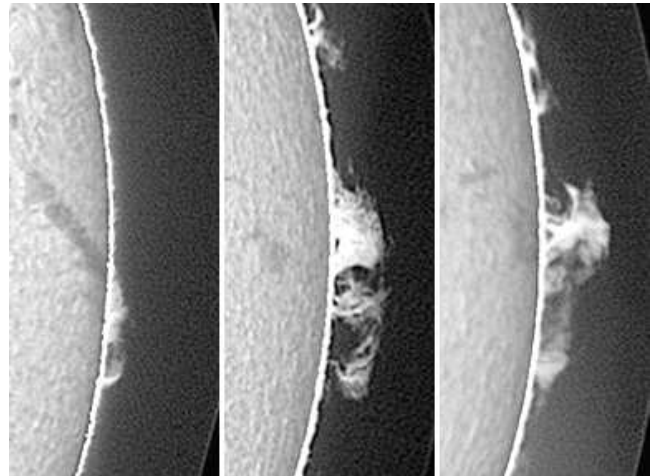


FIG. 1.— Prominence W5N on June 24 (Learnmouth; left), 25 (Big Bear; middle), 26 (Udaipur; right panel); north is up, west is right

The unchanged grating angle allows measurement of the aureola spectra (giving the parasitic light superposing the emission lines) immediately before and after the prominence spectra. In our former sequential observations (Stellmacher & Wiehr, 2017), the change of the grating angle between the Sr II and the Na D exposures required to repeatedly expose aureola spectra and thus alternating the telescope pointing between the prominence and its (emission-free) neighborhood. This method is sensitive to the pointing accuracy and typically requires a time interval of several minutes between the observation of both lines.

ewiehr@gwdg.de, stell@iap.fr, mbianda@irsol.ch

¹ Institut für Astrophysik, D-37077 Göttingen, Germany

² Institut d'Astrophysique, F-75014, Paris, France

³ Istituto Ricerche Solari Locarno, associated with Università della Svizzera italiana, CH-6605 Locarno, Switzerland

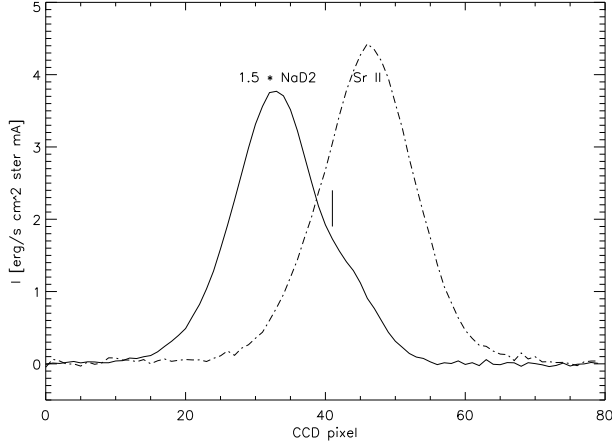


FIG. 2.— Emission lines NaD₂ 5889.95 Å (9th; 8.4 mÅ/px) and Sr II 4077.71 Å (13th order; 5.8 mÅ/px) at a fixed grating angle yielding neighboring locations on the CCD; the H₂O 5890.7 Å blend in the red wing of NaD₂ is indicated by a vertical bar

In the present observations the repetition rate is much shorter due to a 1.5 s switch of the two pre-filters. The dimension of the camera chip allows coverage of both Na D lines. For comparison with former data, we additionally observed on June 26 the neighboring emission lines He I 5015 Å and Fe II 5018 Å, and, separately, H_β 4101 Å. Precise guiding is assured by the accurate monitoring of the Gregory telescope’s primary image (Küveler et al., 2003).

Disk center spectra are not used for wavelength references but rather to calibrate the line intensity in absolute units [erg/(s cm² ster)], using the tables by Labs and Neckels (1970). The spectrograph slit of correspondingly 1.5” width and 120” length was oriented along the direction of refraction (i.e. toward zenith).

2.1. Refraction in Earth’s atmosphere

When comparing spectral lines with a marked wavelength difference (here 1818 Å between Sr II and Na D₁), the spectrograph slit must be precisely oriented along the direction of refraction to ensure that identical solar structures occur in both spectra (shifted perpendicular to the dispersion). This is obtained by orienting the slit along the zenith direction, which, however, rotates over the solar image. As a consequence, a slit oriented toward the zenith sweeps through the solar structures.

The daily variation of the parallactic angle Φ (spanned by the geographic north and zenith direction) depends on the solar decl. D_{sun} (Figure 3). For $D_{sun} \geq 0^\circ$, Φ shows a minimum and a maximum, respectively, at sunrise and at sunset. With increasing D_{sun} these extrema become broader and move apart from the sunrise and the sunset. For $D_{sun} > 20^\circ$ (May, 20 through July, 20) and the 46.17° latitude of IRSOL, the two flat extrema allow orientation of the spectrograph slit at hour angles $-6.0 < \alpha < -3.3$ hr and $+3.3 < \alpha < +6.0$ hr such, that it deviates from the zenith direction by $\leq \pm 1$ (two dotted horizontal lines in Figure 3). This allows taking time-sequence observations up to 2.7 h with an extended slit always covering the same solar structures.

Balthasar & Wiehr (1994) made use of the complete morning minimum for simultaneous observation of Ca II 8498 Å and the line pair He 3888 Å and H₈ 3889 Å in a quiescent

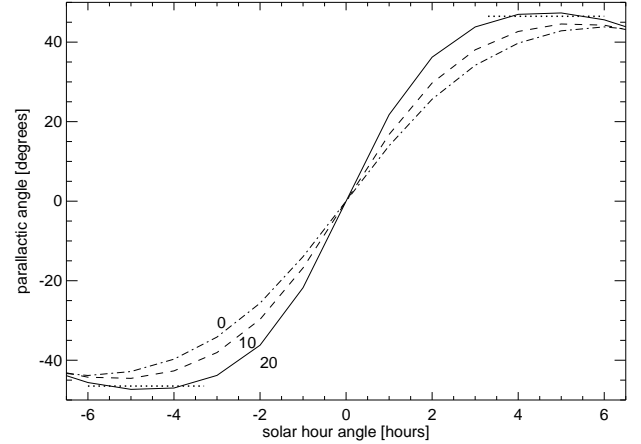


FIG. 3.— Parallactic angle Φ as a function of solar hour angle for the Locarno observatory (at 46.17° latitude) and solar declinations $D_{sun} = 0^\circ$ (dash-points), $D_{sun} = +10^\circ$ (dashes), $D_{sun} = +20^\circ$ (full line); observing windows have $\Phi \approx \text{const.}$ (dotted horizontal lines)

prominence. Anan et al. (2017) observed a similar spectral range of almost 4600 Å from 10:53 to 11:37 local time, where Φ varies considerably. Here, we present observations of Sr II and Na D in a prominence on June 25, during the afternoon maximum and sixteen hours later on June 26, during the morning minimum with a slit orientation toward zenith.

3. DATA REDUCTION

Prominence emission lines are superposed by parasitic light originating from imperfect telescope optics (rather than from Earth’s atmosphere; see Stellmacher & Wiehr, 1970). We take spectra of the “aureola” in the immediate (emission-free) prominence neighborhood with almost the same slit inclination to the solar limb. The so obtained aureole spectra are normalized to the intensity of the prominence background and then subtracted (for details see Ramelli et al., 2012). These do not allow full disappearance of the terrestrial H₂O lines by subtraction. (The reason for this is discussed in Section-3.1.) In particular, remnants of H₂O 5890.7 Å affect the red wing of NaD₂ (Figure 2). For comparison with Sr II we thus prefer NaD₁, which is not affected by terrestrial H₂O lines. We verify that both Na D lines have the same Doppler shifts, and that their integrated line intensities show a fixed relation of $D_2/D_1=1.4$ (in agreement with Landman, 1981).

We spatially average the spectra over 5 rows (1.7”) adapted to the spectrograph slit of correspondingly 1.5” width. For the spatial regions, visually selected to avoid multi-component emissions and marked in Figures 5b and 6b, we determine macro-shifts, V_{LOS} , reduced widths, $\Delta\lambda_D/\lambda_0$, and integrated line intensities, $E = I_0 \times \Delta\lambda_D \times \pi$ (valid for optically thin lines) fitting single Gaussians sequentially to the upper 15%, 40% or 65% of the central intensity. The wavelengths of the emission maxima are determined from the upper 15%. Reduced widths and integrated intensities are only taken from narrow and symmetric line profiles, where the Gaussians at 15%, 40% or 65% of the central intensity are almost identical. This criterion excludes asymmetric profiles; multi-peak profiles are already avoided visually (see above).

3.1. Scaling the wavelengths

As a wavelength reference for Doppler shifts we determine the centers of the Sr II and Na D absorption lines in the aureola at the upper ends of each spectrum at 115'' distance from the limb in slit direction (which corresponds to 80'' above the equatorial west limb accounting for the slit inclination). This reference allows calibration of Doppler shifts independent of the complex photospheric velocity fields at disk center and of ubiquitous drifts of the spectrograph.

In order to connect these wavelengths from the aureola and those at the solar disk, we observe (in 2018 July) aureola spectra of Sr II 4078 Å and Na D₁ at various distances from the limb. We find that the absorption lines in the aureola become increasingly blue and red shifted when approaching the east and west limbs respectively. At the solar poles, these shifts disappear (Figure 4).

The Doppler shifts in the aureola spectra are found to be equal for the Sr II and the Na D line. Their variation along the slit is the same in the aureola and in the emission spectra because the slit inclination is largely preserved. The different colors of both lines indeed affect the aureole continuum intensity, which is considered by normalization.

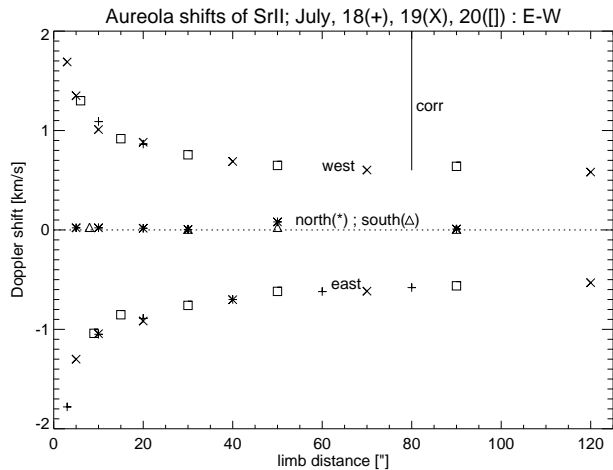


FIG. 4.— Doppler shift of Sr II in the aureola as function of distance from the limb, eastward and westward of the solar equator and northward and southward of the solar poles; the correction to a co-rotating reference is indicated.

Figure 4 indicates that aureola regions closer to the solar disk obtain parasitic light from increasingly smaller segments of the solar sphere, which thus imprint increasing rotational Doppler shifts (they are evidently equal for the Na and the Sr II lines) on the respective aureola spectra. On the other hand, for increasing limb distances, the aureola contains parasitic light from increasingly larger segments, and finally from the half-sphere with a much smaller mean rotational Doppler shift. Near the poles the sphere segments contain no rotational Doppler shifts, and the wavelengths in the aureola then show zero shifts for all limb distances (Figure 4). Hence, the polar aureola gives an almost perfect standard for the calibration of Doppler velocities.

3.2. The co-rotating reference system

Our wavelengths from the upper end of each spectrum (80'' above the limb) may be converted to a co-rotating system. Figure 4 gives for $x=80''$ a shift of $y=0.6$ km/s with respect to the un-shifted polar wavelengths. Assuming 2 km/s rotation,

our velocity scale had to be shifted by -1.4 km/s (marked in Figure 4) to relate it to the photosphere below the prominence.

Since we determine the aureola wavelengths of Sr II 4078 and of Na D at each spectrum of the time series, the resulting macro-velocities are free from spectrograph drifts and from slow terms of spectrograph seeing. The low noise level of the emission lines (see examples in Fig 2) and the Gaussian fit of the upper 15% lead to an estimated accuracy of ≤ 50 m/s for the macro-velocities.

4. RESULTS

The H α slit-jaw images from June 25 show that the prominence appeared quiet without noticeable morphological changes during the 42.7 min time series (Fig 5). In contrast to the slit-jaw images, the aspect of the spectra (lower panels of Figure 5) varies at locations with multi-component emissions, e.g. at the border of the small emission gap in the prominence center. Such multi-components become particularly visible in narrow lines from heavy elements ($\mu_{Sr} = 86.7$) and are often hidden in broad Balmer lines. We select seven spatial scan positions (marked in the lower panels of Figure 5) at regions largely free from multi-components.

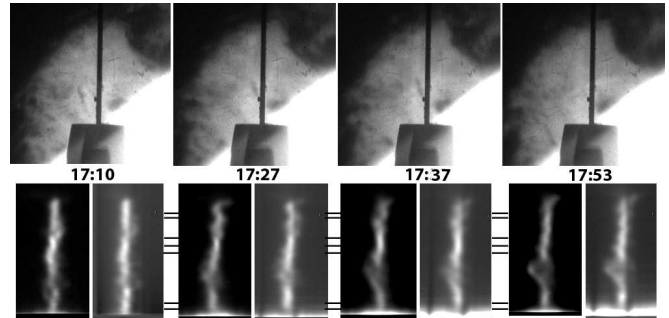


FIG. 5.— Prominence from June 25 at west 5N. Upper panels: H α slit-jaw images at time steps 1, 20, 40, 60; the slit is oriented along the direction of refraction. Lower panels: corresponding spectra of Sr II (left) and Na D₂ (right of each pair); spatial length = 65'' and the bars give the locations of scan rows

On June 26, 16 hr after the June 25 observations, the prominence is less quiet and characterized by an expansion of the central emission gap, which suddenly rose up with a projected motion of ≈ 10 km/s (between 10:04:10 and 10:07:08; see the upper panel of Figure 6). This value is close to the one found by Stellmacher & Wiehr (1973) for a similar event, which also showed large Doppler shifts ≤ 10 km/s at the boundary of the rising cavity. Our spectra even reach 35 km/s. Yet, Sr II and Na D show a striking similarity (see the lower panels of Figure 6), suggesting a common origin within the same resolution element, which we estimate to amount $2'' \times 2''$, or $1500 \text{ km} \times 1500 \text{ km}$ on the sun.

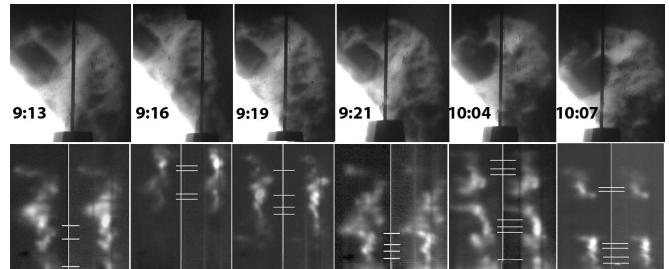


FIG. 6.— Same as in Figure 5, but 16 hr later

4.1. Balmer brightness

H_δ was only observed on June 26. We find a mean integrated intensity $E(H_\delta) = 8350 \text{ erg}/(\text{s cm}^2 \text{ ster})$ that, following the tables by Gouttebroze et al. (1993) for $T=8000 \text{ K}$, corresponds to $\tau_\delta = 0.08$. For June 25, we estimate the H_δ emission assuming the enhancement of 3.8 with respect to June 26, which was measured for NaD_1 , and obtain $\tau_\delta = 0.15$. The H_δ line is thus optically thin on both days.

For H_α the tables give $\tau_\alpha = 4.0$ and 9.5 , respectively, and $E(H_\alpha) = 23$ and $38 \times 10^4 \text{ erg}/(\text{s cm}^2 \text{ ster})$. Assuming for an elementary volume $E(H_\alpha) = 1 \times 10^4 \text{ erg}/(\text{s cm}^2 \text{ ster})$ (see Stellmacher & Wiehr, 2000, and references therein) the resolution area covers, respectively, 23 and 38. Even the larger number is compatible with a single layer of $\phi \leq 240 \text{ km}$ elements in the line of sight and favors the single line approximation as in Stellmacher & Wiehr (2017). The spectra show, indeed, moments where narrower lines coincide with higher line-center intensities, as expected from the relation $E = I_0 \times \Delta\lambda_D \times \pi$ for optically thin lines.

4.2. Time variation of the Doppler shifts

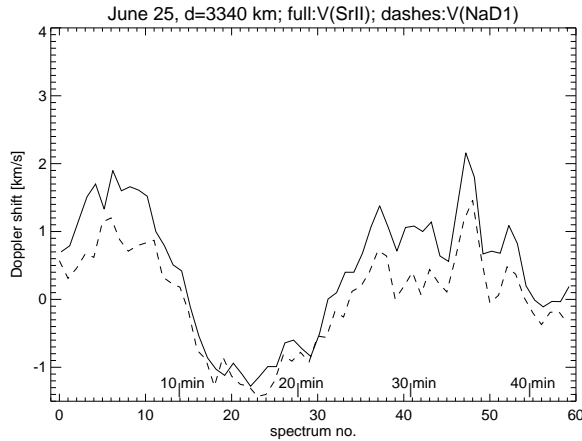


FIG. 7.— Velocity variation of Sr II (full line) and NaD_1 (dashes) velocities with respect to the photosphere beneath the prominence for the 60 steps of the time-series from June 25 in the lowest scan row at $d=3340 \text{ km}$ from the solar limb in the slit direction

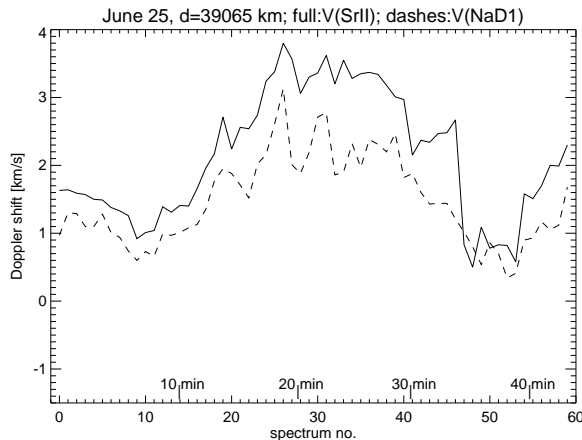


FIG. 8.— Same as Figure 7 but for the uppermost scan row at $d=39065 \text{ km}$ from the solar limb in the slit direction; the ordinate scales of Figures 7 and 8 are made equal for a direct comparison

Figures 7 and 8 show the V_{LOS} obtained from Sr II and NaD_1 for the 60 spectra of the time-series in the lowest and the highest scan rows on June 25 (marked in Figure 5). They are located at $3,860 \text{ km}$ and at $39,600 \text{ km}$ from the solar limb in slit direction. The time-series (Figures 7 and 8) show wave-like velocity variations with a period of $\approx 30 \text{ min}$ for both lines. The V_{LOS} are synchronous in Sr II and NaD_1 with phase shifts smaller than the 42.7 s time step, their amplitudes are systematically higher for Sr II than for NaD_1 . In Figure 9 we compare the Sr II velocities at lower, middle, and upper locations in the prominence on June 25. The temporal velocity means indicate an increase from 0.4 via 1.5 to 2.1 km/s through the three levels, whereas the oscillation amplitude remains almost constant. This indicates that the oscillation is superposed on an general red-shift, which increases with height. The oscillation extrema move along the slit direction with $20\text{-}40 \text{ km/s}$.

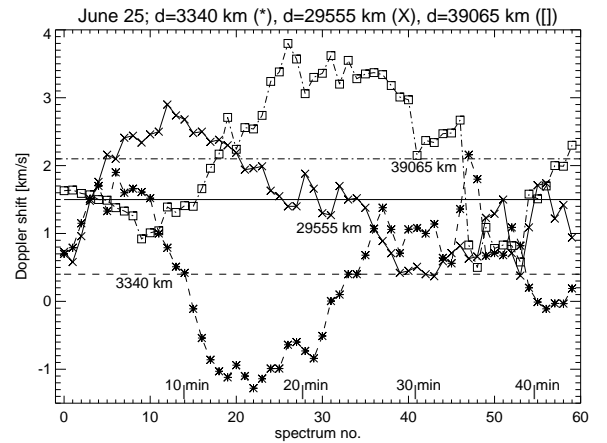


FIG. 9.— Time variation of Sr II velocities in the prominence from June 25, for the 60 spectra at $d=3340 \text{ km}$ (dashes), at $d=29555 \text{ km}$ (full line) and at $d=39065 \text{ km}$ (dashed points) from the solar limb in the slit direction; the ordinate scale for all scans is the same as in Figures 7 and 8

4.3. Velocity excess of ions

In Figure 10 we show the scatter-plot of LOS velocities of Sr II and NaD_1 in the co-rotating system (see Sec. 3.2) for the 60 spectra of the time series in the 7 spatial cuts (see Figure 5).

From these 420 spectra we obtain a net shift excess of $V_{LOS}(\text{Sr II}) = 1.22 \pm 0.02 \times V_{LOS}(\text{NaD}_1)$. Concerning the error range, we note that the Gaussian fit to the low-noise spectra (see Fig 2) will not markedly affect the accuracy. We consider the scatter in Figure 10 to be due to different influence of image motion in the quasi-simultaneous Sr II and NaD spectra.

For June 26, we find from 41 scans in the 6 spectra (Figure 6) velocity excess $V_{LOS}(\text{Sr II}) = 1.10 \pm 0.03 \times V_{LOS}(\text{NaD}_1)$ (Figure 11). This sample is smaller than on June 25 but contains higher values, notably near the rising cavity (see Figure 6). For the neighboring lines $\text{Fe II } 5018 \text{ \AA}$ and $\text{He I } 5015 \text{ \AA}$ (singlet line) we find from 27 symmetric profiles a velocity excess of $V_{LOS}(\text{Fe II}) = 1.12 \pm 0.05 \times V_{LOS}(\text{HeD}_1)$. The slight ordinate displacement relative to the Sr II - NaD data (Figure 11) may arise from the missing reference wavelength of the He line, which does not exist in the aureola spectrum and was taken from the Fe II line via the dispersion. The identical slopes for both line pairs in Figure 11 indicate that the velocity excess of ions has actually diminished 16 hr after the

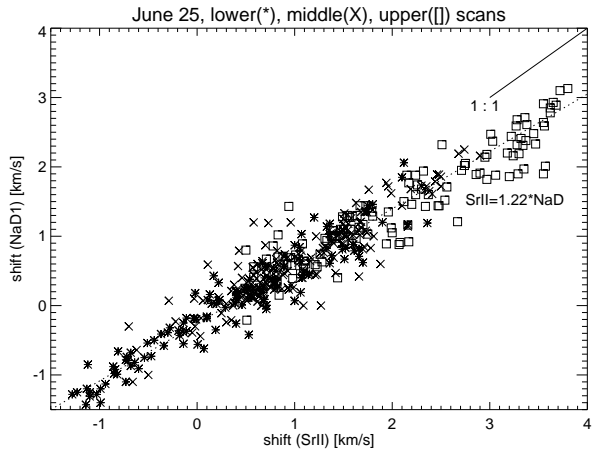


FIG. 10.— Scatter plot of 420 V_{LOS} of Sr II and Na D₁ from the 7 scan rows and 60 time steps for June 25; the plot shows that the Sr II velocities are 1.22 ± 0.01 times larger than those of Na D

observation of the time-series, and that the excess is a standard behavior for ions with respect to neutrals.

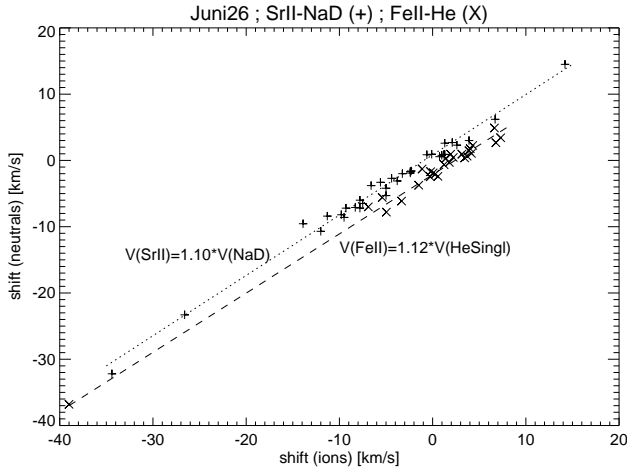


FIG. 11.— Scatter plot of 41 V_{LOS} of Sr II and Na D₁(+) and 27 V_{LOS} of Fe II 5018 Å and He I 5015 Å (X) for June 26; the ion velocities are 1.11 ± 0.05 times larger than those of the neutrals; the ordinate displacement of V_{LOS} (He) reflects the missing reference wavelength in the aureola spectrum

4.4. Integrated line intensities and electron density

The ratio of total line intensity, $E_{tot}(\text{Na D})/E_{tot}(\text{Sr II})$, in Figure 12 does not show the 30 min period of V_{LOS} (see Figures 7-9). It is thus largely independent of macro-shifts. Possible variations of smaller periods cannot be established with sufficient significance. In Figure 13 we plot the observed range of emission ratio versus the distance from the solar limb in the slit direction and obtain a constant mean of 0.68.

The ratio of total line intensity, $E_{tot}(\text{Na D})/E_{tot}(\text{Sr II})$, allows estimation of the electron density. Converting the Na D₁ emissions into Na D₂ emissions with the factor $E(D_2)/E(D_1)=1.4$ (Sec.3), we obtain from the mean $E(\text{Na D}_1)/E(\text{Sr II})=0.68 \pm 0.1$, the value $E(\text{Na D}_2)/E(\text{Sr II})=0.95 \pm 0.1$ for June 25. Applying the calculations by Landman (1983) for $T=8000$ K and $V_{nth} = 3$ km/s and the correction factor 0.5 (Landman, 1986), this ratio gives $n_e = 4 \cdot 10^{10} \text{cm}^{-3}$, which is the same as that found by Stellmacher & Wiehr (2017).

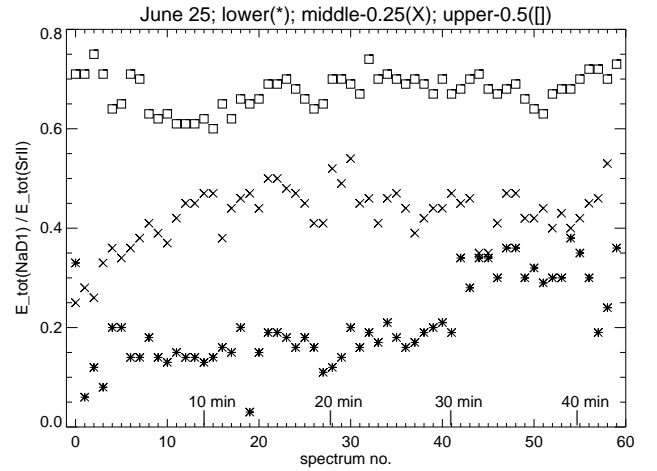


FIG. 12.— Emission ratio $E(\text{Na D}_1) / E(\text{Sr II})$ for the 60 spectra from June 25 at a lower (stars), middle (X-signs), and upper locations (squares) vertically displaced by 0, -0.25, and -0.5 for clearness

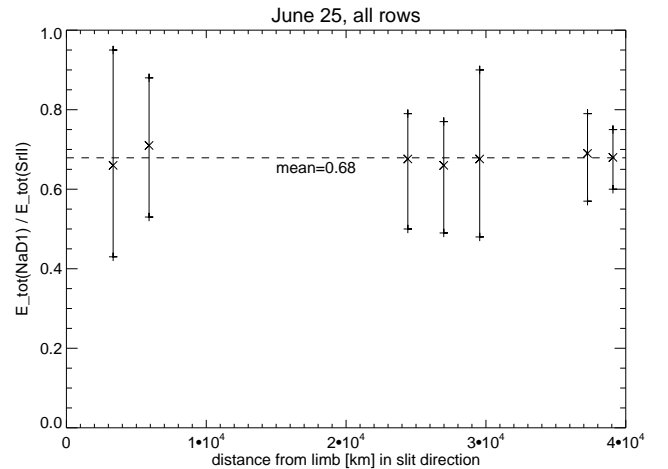


FIG. 13.— Mean emission ratio of Na D₁ and Sr II for all 7 scan rows on June 25 as a function of distance from the limb in slit direction

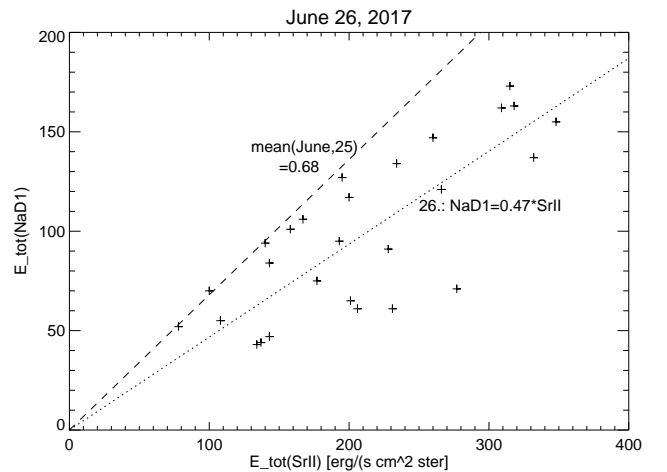


FIG. 14.— Relation between integrated line intensity of Na D₁ and Sr II for 28 profiles from June 26, at the spatial locations marked in Figure 6; all of them are located below the mean relation for June 25 (0.68, dashed line); the mean relation on June 26 is 0.47 ± 0.2

On June 26, the prominence shows fainter mean emissions; $E(\text{Na D}_1)$ reduces by ≈ 3.8 , but $E(\text{Sr II})$ only by ≈ 2.5 . As a

consequence, the mean emission ratios are generally smaller than those on June 25. The 28 line profiles, unaffected by multi-component emissions (spatial positions marked in the lower panel of Figure 6), give a wide range of emission ratios $0.25 \leq E(\text{Sr II})/E(\text{Na D}_1) \leq 0.7$ (Figure 14), almost entirely below the mean of 0.68 found for June 25. The range of ratios gives $1 < n_e [10^{10} \text{cm}^{-3}] < 4$, indicating smaller n_e values on June 26, than on June 25.

4.5. Width excess of the Sr II line

From symmetric and narrow emissions (i.e. unbiased by multi-component emissions) we find mean reduced widths $\Delta\lambda_D/\lambda_0(\text{Sr}) = 0.95 \cdot \Delta\lambda_D/\lambda_0(\text{Na})$. The Doppler formula, $\Delta\lambda_D/\lambda_0 = 1/c \cdot \sqrt{2 R T_{kin}/\mu + V_{nth}^2}$, however, leads, for the atomic mass $\mu(\text{Na}) = 23$ and $\mu(\text{Sr}) = 87.6$, to a markedly smaller ratio of $\sqrt{23/87.6} = 0.51$ thus indicating an excess broadening of the Sr II line. $\Delta\lambda_D/\lambda_0(\text{Sr II})$ does not depend on the macro-velocities V_{LOS} (Figure 15). This is equally found for Na D₁, and also on June 26, even for the larger shifts occurring during the activated phase; it agrees with Engvold (1972). The observed range $1.0 \leq \Delta\lambda_D/\lambda_0 [10^{-5}] \leq 1.4$ gives non-thermal velocities (i.e. for $T_{kin} = 0 \text{K}$) of $3.0 \leq V_{nth} \leq 4.2 \text{km/s}$.

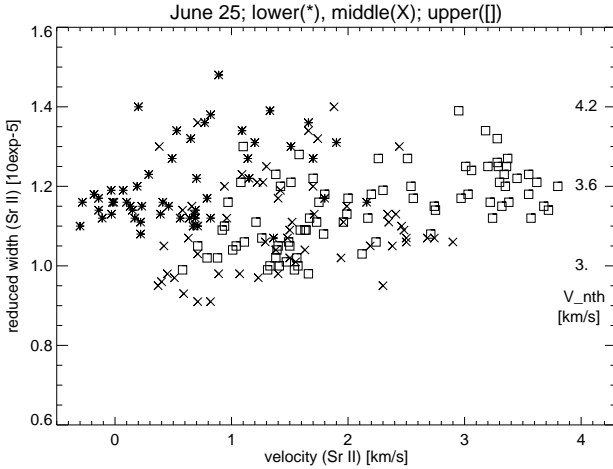


FIG. 15.— Relation between reduced widths and Doppler shifts of Sr II on June 25 for symmetric narrow profiles in the lower, middle, and upper scan rows (same as in Figure 9)

5. CONCLUDING COMMENTS

5.1. The systematic velocity excess of ions over neutrals

The data presented here confirm at higher accuracy the net drift excess of ions over neutrals observed by Stellmacher & Wiehr (2017). This systematic velocity excess differs from that of Ca II 8542 Å over He I 10830 Å, which was found by Khomenko et al. (2016) at moments of high velocities in short-lived small areas. Our result may in part be due to the judicious choice of the emission lines Sr II 4078 Å and Na D, which are optically thin and narrow, and to the fact that we analyzed a quiet prominence. The smaller velocity excess of 1.11 found for June 26, might be due to a different degree of ionization, as is indicated from the smaller ratio of integrated line intensities (see Figure 14) or to a different density in the activated phase of the prominence.

5.2. The electron density

The estimate of n_e is based on the assumption that Sr II 4078 Å and Na D₂ originate in the same emission area. The visual aspects of the spectra (lower panels of Figures 5 and 6) is in favor of such a common origin. The small optical thickness ($\tau(H_\delta) \leq 0.15$) and the small geometric extension of a single layer thickness (see Section 4) indicate a line formation in the same plasma volume. The variation of the emission ratio through the observing time (Figure 12) does not show the 30 min variation of v_{LOS} (see Figure 7 - 9), indicating that the electron density n_e is not related to the macro-velocities. The constancy of n_e with height (Figure 13) is in accordance with our earlier findings (Stellmacher & Wiehr, 2015, 2017). For the smaller n_e on June 26, a possible relation between the brightness decrease and/or the activation of the prominence on June 26 remains unsolved.

5.3. The non-thermal line-broadening

The width excess of the Sr II over the Na I profiles is in accordance with Ramelli et al. (2012) and Stellmacher & Wiehr (2015, 2017) who found emission lines from ions to be systematically broader than those from neutrals. The conjecture that this width excess may be related to the excess of ion velocities seems not to be confirmed by the results in Figure 15. Hence, the systematic width excess of lines from ions still remains unclear.

5.4. The oscillatory behavior of the Doppler velocities

The time-series show a wave-like velocity variation with $\approx 30 \text{min}$ period, which is highly synchronous for ions and neutrals, in agreement with Balthasar et al. (1993), Balthasar & Wiehr (1994), Khomenko et al. (2016) and Anan et al. (2017). If we follow that period through the scan rows, it seems to travel along the slit direction with a velocity decelerating from 40 km/s in the lower to 20 km/s in the upper scan rows. The superposed increase of a mean red-shift (Figure 9) suggests a swaying motion of the prominence as a whole (see Okamoto et al., 2015). Concerning its origin, Wedemeyer et al (2013), Hillier et al. (2013) and Wedemeyer & Steiner (2014) showed that the weak prominence magnetic field responds to ubiquitous motions of its photospheric footpoints. In this scenario, the motion of ions is directly exerted by the Lorentz force, and the motion of the neutrals arises from friction to the ions.

6. ACKNOWLEDGMENTS

We thank Dr. R. Ramelli (IRSOL) for suggestions with data reduction and fruitful discussions, and D. Gisler (IRSOL) for developing the device to shift the pre-filters. Drs. R. Hessman (IAP Göttingen) and B. Inhester (MPS Göttingen) contributed helpful comments. E.W., G.S. thank IRSOL for hospitality. IRSOL is supported by the Swiss Confederation (SEFRI), Canton Ticino, the city of Locarno, and the local municipalities. We are indebted to the unknown referee for carefully reading our manuscript and providing helpful hints to improve it.

7. REFERENCES

- Anan T., Ichimoto K., & Hillier A. 2017, A&A 601, A103 (DOI 10.1051/0004-6361/201629979)
 Ballester, J.-L., Alexeev, I., Collados, M., Downes, T., Pfaff, R.-F., Gilbert, H., Khodachenko, M., Khomenko, E.,

- Shaikhislamov, I.-F., Soler, R., Vázquez-Semadeni, E., & Zaqarashvili, T. 2018, *SSRv*, 214, 58 (DOI 10.1007/s11214-018-0485-6)
- Balthasar, H., Wiehr, E., & Schleicher, H., Wöhl, H. 1993, *A&A*, 277, 635
- Balthasar, H., Wiehr, E. 1994, *A&A*, 286, 639
- Envold, O. 1972, *Solar Phys.*, 23, 346
- Gilbert, H. R., Hansteen, V. H., Holzer, T. E. 202, *ApJ*, 577, 464
- Gouttebroze, P., Heizel, P., & Vial, J.-C. 1993, *A&A*, Supl. 99, 513
- Hillier, A., Morton, R. J., & Erdélyi, R. 2013, *ApJ*, 779, L16 (DOI 10.1088/2041-8205/779/2/L16)
- Khomenko, E., Collados, M., & Diaz, A.J. 2016, *ApJ*, 823, 132 (DOI 10.3847/0004-637X/823/2/132)
- Küveler, G., Wiehr, E., & Bianda, M. 2003, *AN*, 324, 308 (DOI 10.1002/asna.200310105)
- Labs, D. & Neckels, H. 1970, *Solar Phys.*, 17, 50
- Landman, D. A. 1981, *ApJ*, 251, 768
- Landman, D. A. 1983, *ApJ*, 269, 728
- Landman, D. A. 1986, *ApJ*, 305, 546
- Okamoto, T.J., Antolin, P., De Pontieu, B., Uitenbroek, H., Van Doorselaere, T., & Yokoyama, T. 2015, *ApJ*, 809, 71 (DOI 10.1088/0004-637X/809/1/72)
- Ramelli, R., Stellmacher, G., Wiehr, E., Bianda, M. 2012, *Solar Phys.* 281, 697 (DOI 10.1007/s11207-012-0118-2)
- Stellmacher, G. & Wiehr, E. 1970, *A&A*, 7, 432
- Stellmacher, G. & Wiehr, E. 1973, *A&A*, 24, 321
- Stellmacher, G. & Wiehr, E. 2000, *Solar Phys.*, 196, 357 (DOI 10.1023/A1005237823016)
- Stellmacher, G. & Wiehr, E. 2015, *A&A* 581, 141 (DOI 10.1051/0004-6361/201322781)
- Stellmacher, G. & Wiehr, E. 2017, *Solar Phys.*, 292, 83 (DOI 10.1007/s11207-017-1103-6)
- Wedemeyer, S., Scullion, E., Rouppe van der Voort, L., Bosnjak, A., & Antolin, P. 2013, *ApJ*, 774, 123 (DOI 10.1088/0004-637X/774/2/123)
- Wedemeyer, S. & Steiner, O. 2014, *PASJ*, 66S, 10 (DOI 10.1093/pasj/psu086)